ELSEVIER

Medical Image Analysis 7 (2003) 65–78

MEDICAL IMAGE ANALYSIS

www.elsevier.com/locate/media

Recovering the X-ray projection geometry for three-dimensional tomographic reconstruction with additional sensors: Attached camera versus external navigation system

M. Mitschke[a,*], N. Navab[b]

[a]*Siemens AG Medical Solutions, Henkestrasse 127, 91052 Erlangen, Germany*
[b]*Siemens Corporate Research, 755 College Road East, Princeton, NJ 08540, USA*

Received 7 September 2001; received in revised form 25 February 2002; accepted 19 April 2002

Abstract

Three-dimensional tomographic reconstruction using intra-operative mobile C-arms could provide physicians with new and exciting tools for image-guided surgery. Recovery of the projection geometry of mobile X-ray systems is a crucial step for such reconstruction procedures. Recent work on medical imaging describes the use of optical or electro-magnetic sensor systems in order to navigate surgical instruments. These systems can also be used for the estimation of C-arm motion, and therefore for the recovery of the projection geometry of the X-ray C-arm. In this case, the mathematical problem that needs to be solved is equivalent to the hand–eye calibration well studied by both the computer vision and robotics community. We first study the recovery of the motion and projection geometry using five different hand–eye calibration methods proposed in the literature. The optical navigation system POLARIS from Northern Digital Inc. was used in our experiments. The results of the estimated motion and projection geometry using the five hand–eye calibration methods are compared with the same results obtained using an off-the-shelf CCD camera attached to the mobile C-arm. The experimental results include three-dimensional tomographic reconstruction results using our mobile C-arm. We show that even though the motion of the C-arm is more precisely recovered using the navigation system, the projection geometry is better estimated using the attached CCD camera.

Keywords: X-ray projection geometry; Three-dimensional tomographic reconstruction; Sensors; External navigation system

1. Introduction

The real-time recovery of the projection geometry is a fundamental issue in various applications. In particular, both the medical imaging and augmented reality communities are interested in this subject. In augmented reality applications the goal is to merge virtual objects onto real images as the viewer is moving and therefore changing her/his viewpoint (Tamamura et al., 1999; Azuma, 1997; ImageOverlay, 1998; Hoff, 1998). Other than for augmented reality applications, the medical imaging community is interested in real-time recovery of the X-ray projection geometry for three-dimensional (3D) tomographic reconstruction. Both of these scientific communities show great interest in using precise and commercially available external optical tracking and localization systems such as Optotrak and Polaris from Northern Digital, Inc. (Northern Digital, 2001). These external sensors have been used in many medical (Wells et al., 1998; Delp and Colchester, 1999; Delp et al., 2000) and augmented reality applications (Birkfellner et al., 1998, 2000) in recent years. In addition to optical navigation systems, there is a large number of electro-magnetic, mechanical, and ultra-sonic navigation systems in exist-

*Corresponding author. Tel.: +49-9131-84-4516; fax: +49-9131-84-4771.
E-mail address: matthias.mitschke@siemens.com (M. Mitschke).

1361-8415/02/$ – see front matter
PII: S1361-8415(02)00091-9

ence. Due to practicability and accuracy issues they are not as widely used as optical systems.

Tomographic reconstruction has been widely studied (Kak et al., 1977; Tuy, 1983; Feldkamp et al., 1984; Kruger et al., 1987). Three-dimensional angiography, the tomographic reconstruction of high-contrast objects such as contrast-agent-enhanced blood vessels, has gained increasing interest in recent years (Koppe et al., 1997; Navab et al., 1998; Trousset et al., 1999) and has led to many successful products. For these tomographic reconstructions, a set of two-dimensional (2D) X-rays is aquired during a 200° rotation around the patient. Thus far, this has been done using stationary C-arm systems. With the availability of mobile iso-centric X-ray C-arm systems, the focus is now on the use of these rather inexpensive systems for tomographic reconstruction. The characterization of the projection geometry of the 2D X-ray images is the crucial point for 3D reconstruction.

Extending our previous work (Mitschke and Navab, 2000a), we first discuss the mathematical equations that need to be solved in order to use an external sensor for tracking and localization. We use the recovery of the projection geometry for interventional 3D tomographic reconstruction as an example.

We show that the mathematical framework is the same as the well-known hand–eye calibration framework of the computer vision and robotics community (see Daniilidis, 1999, for an overview). The position and orientation of the camera with respect to the gripper of the robot, to which it is attached, is determined with this calibration method. We use it to recover the motion of the C-arm and therefore the X-ray projection geometry during a rotational run around an object of interest. The results are evaluated both in terms of a qualitative comparisons of 3D reconstruction results and a numerical comparison of motion estimation parameters. Five different hand–eye calibration methods are evaluated.

We then compare the results of the hand–eye calibration methods mentioned above with that obtained using an integrated standard CCD camera (see Navab et al., 1999a). We discuss the interesting observation that even though the motion parameters are better estimated using the external sensor, the projection geometry is more accurately estimated by the integrated optical camera.

The remainder of the paper is organized as follows. Section 2 provides a general description of the problem of geometrical calibration for 3D tomographic reconstruction. This is taken as the application example in this paper. Note that, for head-mounted display (HMD) calibration, the framework is quite similar. Section 3 first briefly describes the projection geometry for camera and X-ray imaging, and defines the world, camera, external sensor and X-ray coordinate systems. It then introduces the different calibration procedures and the algorithms used. Section 5 presents the experimental results. Conclusions and suggestions for future work are presented in Section 6.

2. Geometric calibration of an X-ray C-arm for 3D tomographic reconstruction

For tomographic reconstruction, a sequence of images is captured during the C-arm rotation around the object of interest. For each image the precise projection geometry has to be determined for the 3D reconstruction process (Navab et al., 1996, 1998; Koppe et al., 1997; Trousset et al., 1999). Most existing C-arms do not provide an accurate projection geometry or pose information. Therefore, the projection geometry has to be calibrated for each image frame.

In order to obtain the most accurate estimation of the projection geometry for each X-ray frame, a calibration phantom with X-ray-opaque markers has to be used. It is positioned such that it is visible in each frame. The projection matrix representing the projection geometry can then be estimated from the set of detected markers in the X-ray image and the corresponding 3D model points. We use the projection matrices obtained by this method as the *gold standard*—all other methods are compared to it—for our evaluation experiments.

Using this very precise calibration method in real medical applications results in the problem that both the marker points and the object that is to be reconstructed have to be visible in the sequence of X-ray images. Marker points that overlay the object (patient's anatomy) influence the result of the 3D reconstruction. Vice versa, the pattern recognition process for precisely locating the markers in the X-ray image is influenced by the overlaid object of interest.

To overcome this problem, recovery of the projection geometry can be done in an off-line procedure if the motion of the C-arm is reproducible between the calibration and the patient run (Navab et al., 1998; Trousset et al., 1999). Some C-arm systems, however (depending on the mechanical design and the reproducibility of their motion), do not have this desirable property. The projection geometry then has to be determined on-line during the patient run. This is described in more detail in the next section.

3. On-line recovery of the projection geometry

In this section we define the framework for the on-line recovery of the X-ray projection geometry from external sensors. First, we briefly introduce the X-ray projection geometry and the concept of the virtual detector plane. Then the two different approaches, integrated CCD camera and external navigation system, compared in this paper are presented.

3.1. Definition of the X-ray projection geometry

Often, after image distortion correction, the C-arm

projection geometry is approximated by a pinhole camera model (Rougée et al., 1993; Koppe et al., 1995; Navab et al., 1996, 1998). This model is commonly used for optical cameras. Here we consider a mobile C-arm equipped with a (distortion-free) solid-state flat panel detector, so no distortion correction is necessary. For distortion correction algorithms, see (Fahrig et al., 1997; Groneschild, 1997).

The X-ray projection geometry is represented by $\boldsymbol{P} \in \mathbb{R}^{3\times4}$, an homogeneous matrix of projection.

$$u \cong \boldsymbol{P} \cdot x, \tag{1}$$

where $u = [u,v,1]^{\mathrm{T}}$ and $x = [x,y,z,1]^{\mathrm{T}}$ are the homogeneous coordinates of an image pixel (2D) and the corresponding 3D voxel of the world coordinate system. The symbol $\cong$ is used to emphasize that the equality is up to scale. This matrix $\boldsymbol{P}$ represents all the imaging geometry parameters, which can be divided into two sets. The first set is called the extrinsic parameters, described by the homogeneous transformation matrix $\boldsymbol{T} \in \mathbb{R}^{4\times4}$. They define the position ($\boldsymbol{t}$) and orientation ($\boldsymbol{R}$) of the imaging system in the world coordinate system. The second set is called the intrinsic parameters and is described by the matrix $\boldsymbol{A} \in \mathbb{R}^{3\times4}$. These parameters depend only on the internal parameters of the imaging system.

$$\boldsymbol{P} = \boldsymbol{A} \cdot \boldsymbol{T} = \begin{bmatrix} \alpha_u & 0 & u_0 & 0 \\ 0 & \alpha_v & v_0 & 0 \\ 0 & 0 & 1 & 0 \end{bmatrix} \cdot \begin{bmatrix} \boldsymbol{R} & \boldsymbol{t} \\ \boldsymbol{0}^{\mathrm{T}} & 1 \end{bmatrix}. \tag{2}$$

It is interesting to note that the intrinsic parameters of a moving X-ray system in general depend on its extrinsic parameters. In the next section we describe this point in more detail and propose the use of the virtual detector concept introduced by Navab et al. (1999a) in order to fix the intrinsic parameters for the X-ray imaging system.

3.2. Virtual detector plane

Due to the weights of both the X-ray source and the detector, the C-arm will undergo minor torsion during motion. Because of this and the large distance between *the* center of projection (X-ray source) and *the* image plane (detector) the intrinsic parameters will not be as constant as assumed for standard CCD cameras. In fact, they depend on the extrinsic parameters of the imaging system.

Fig. 1 demonstrates the differences between the projection geometry for a CCD camera and an X-ray system. The intrinsic parameters of a CCD camera depend only on the manufacturing of the camera and the relation between the image plane, focal point, and optical axis remains fixed. For an X-ray imaging system, the focal point (X-ray source) and image plane (X-ray detector) are far apart from each other, and the optical axis (normal dropping from the X-ray source onto the detector plane) depends on the orientation of the detector plane. Especially if the X-ray

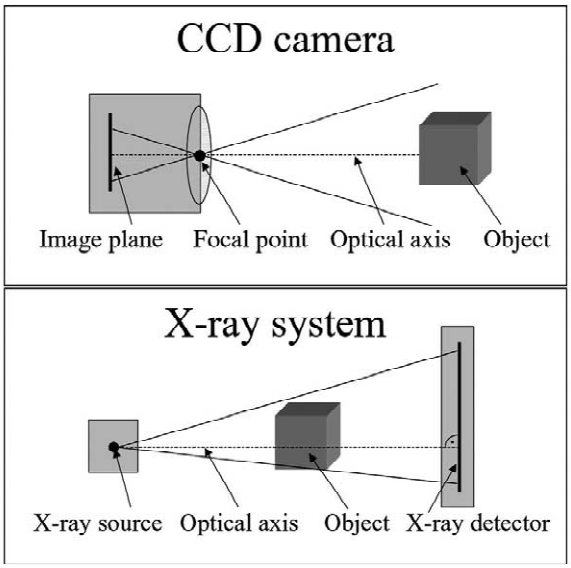

Fig. 1. Pinhole camera model: differences between a CCD camera (top) and an X-ray imaging system (bottom).

system is moving, the intrinsic parameters according to the pinhole camera model are not fixed, and thus cannot be determined once and assumed constant thereafter.

In order to use the framework of hand–eye calibration we need to ensure that our X-ray imaging system can be treated as a regular pinhole camera. We found a solution to solve this problem by introducing the concept of a *virtual detector plane* (Navab et al., 1999a; Navab, 2001). We use a small number of markers on a plate that is attached to the X-ray source (see Fig. 2). Note that, for our experiments, the markers have been arranged such that they do not overlay the markers of the calibration phantom. For a real application these markers are projected close to the borders of the X-ray image, such that they can be easily removed before the reconstruction process. Applying an image transformation (warping) we can force the projected markers to appear in the image at pre-defined positions. We thereby define a virtual image plane with constant intrinsic parameters for all images of the series.

The warping is described by a 2D–2D planar transformation, $\boldsymbol{H} \in \mathbb{R}^{3\times3}$. Instead of actually modifying the images—which would be a time-consuming procedure—the planar transformation can be combined with the original projection matrix in order to obatin a projection matrix with the modified intrinsic geometry.

$$\boldsymbol{P}_i^{\mathrm{VD}} := \boldsymbol{A}^{\mathrm{VD}} \cdot \boldsymbol{T}_i = (\boldsymbol{H}_i \cdot \boldsymbol{A}_i) \cdot \boldsymbol{T}_i = \boldsymbol{H}_i \cdot \boldsymbol{P}_i. \tag{3}$$

The fixed intrinsic parameters are represented by $\boldsymbol{A}^{\mathrm{VD}}$. Thus, the projection geometry for frame i with fixed intrinsic parameters, described by $\boldsymbol{P}_i^{\mathrm{VD}}$, can be computed from the original projection geometry $\boldsymbol{P}_i$.

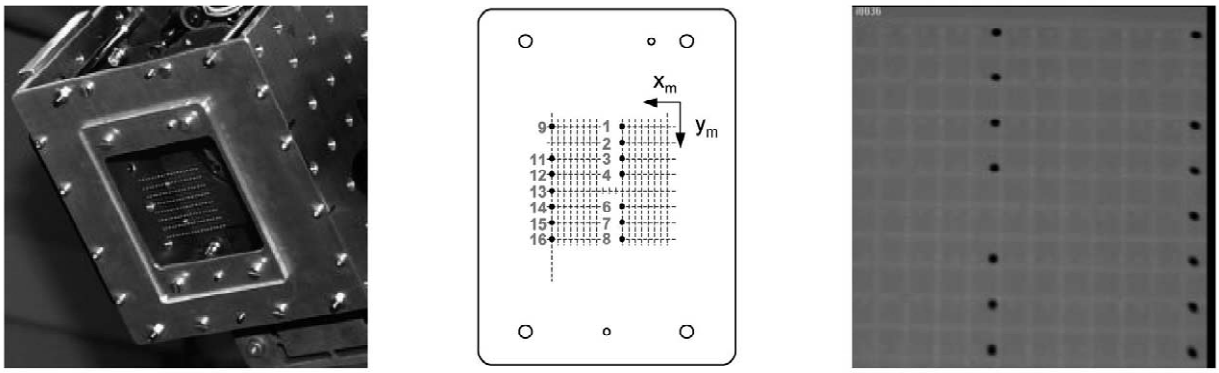

Fig. 2. *Virtual detector plane*: a marker plate attached to the X-ray source (left), CAD drawing of the marker plate (center), and sample X-ray image (right).

3.3. General concept

We now present the necessary components for a unified framework for recovering the projection geometry.

1. *Virtual detector:* We need to model the X-ray imaging system by a pinhole camera model. The problem and the solution to it are described in detail in Section 3.2. The resulting 2D–2D planar transformation $\boldsymbol{H}_i$ is applied to ensure fixed intrinsic parameters throughout the image sequence.
2. *Reference frame:* For one arbitrary image frame the projection geometry is determined simultaneously for both the X-ray ($\boldsymbol{P}^{\mathrm{X}}_{\mathrm{ref}}$) and the sensor system that is used for the on-line calibration procedure ($\boldsymbol{P}^{\mathrm{S}}_{\mathrm{ref}}$).
3. *Motion estimation:* The motion between the current and the reference frame, described by $\boldsymbol{M}^{\mathrm{S}}_i \in \mathbb{R}^{4\times4}$, is computed using the sensor system for on-line calibration. This motion, which is defined in the sensor world coordinate system, then has to be transformed into the world coordinate system, resulting in the motion $\boldsymbol{M}^{\mathrm{X}}_i \in \mathbb{R}^{4\times4}$.

Combining these components leads to the following computation of the X-ray projection matrix $\boldsymbol{P}^{\mathrm{X}}_i$:

$$\boldsymbol{P}^{\mathrm{X}}_i = \boldsymbol{H}_i \cdot \boldsymbol{P}^{\mathrm{X}}_{\mathrm{ref}} \cdot \boldsymbol{M}^{\mathrm{X}}_i, \text{ with } \boldsymbol{P}^{\mathrm{S}}_i = \boldsymbol{P}^{\mathrm{S}}_{\mathrm{ref}} \cdot \boldsymbol{M}^{\mathrm{S}}_i. \tag{4}$$

The motion estimation is the only part that will be different for the various approaches. The following sections describe the application of the developed framework to two methods: using an integrated CCD camera or using an external tracking system.

3.4. Camera-augmented mobile C-arm (CAMC)

This method for the recovery of the projection geometry was presented in (Navab et al., 1999a). A CCD camera is attached to the X-ray source of the C-arm (see Fig. 3).

An optical marker system—not visible in the X-ray image—is used to determine the projection geometry of the CCD camera for each frame. The calibration phantom and a close-up of the marker codes are shown in Fig. 3. The reference projection matrices for the X-ray and CCD camera are determined using a combined optical and X-ray calibration phantom. The motion between the current and the reference frame is computed from the estimated CCD camera projection matrices (see Appendix A for details on the robust computation of motion from projection matrices). Both marker systems are defined in the same world coordinate system. Thus, the motion estimated from the CCD camera projection matrices can be directly applied to the reference X-ray projection matrix ($\boldsymbol{M}^{\mathrm{X}}_i = \boldsymbol{M}^{\mathrm{S}}_i$).

3.5. Recovering the projection geometry using external tracking systems

We used the opto-electronic tracking system POLARIS from Northern Digital, Inc. (2001) in our experiments. This system consists of a double CCD camera system and marker plates with infrared LEDs. One such marker plate, also called the *tool plate*, is attached to the C-arm. Its

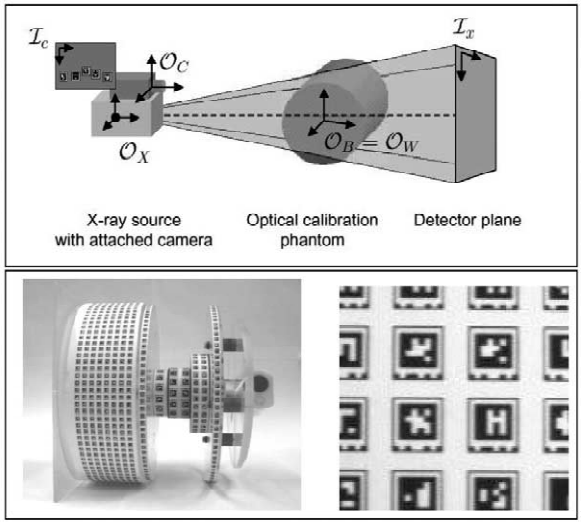

Fig. 3. Schematic setup of the CAMC system (top), the optical calibration phantom and the marker code (bottom).

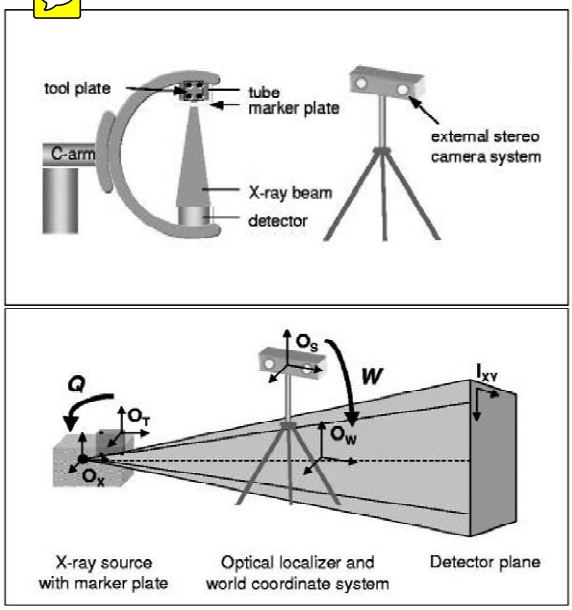

Fig. 4. Schematic setup of our test system (top) and relations between the coordinate systems used (bottom).

position $\boldsymbol{t}$ and orientation $\boldsymbol{R}$ relative to the stereo camera system is tracked with high accuracy in real time. This transformation from sensor coordinate system $\boldsymbol{O}_{\mathrm{S}}$ to tool plate coordinate system $\boldsymbol{O}_{\mathrm{T}}$ is described by a 4×4 matrix of homogeneous coordinate transformations and will be denoted by $\boldsymbol{S}$.

The tool plate is rigidly attached to the frame of the X-ray source. The relation between the X-ray coordinate system $\boldsymbol{O}_{\mathrm{X}}$ and $\boldsymbol{O}_{\mathrm{T}}$ is described by the homogeneous transformation $\boldsymbol{Q}$. The sensor coordinate system $\boldsymbol{O}_{\mathrm{S}}$ and the world coordinate system $\boldsymbol{O}_{\mathrm{W}}$ have a fixed relation during the calibration setup which is described by the homogeneous transformation $\boldsymbol{W}$. See Fig. 4 for a visualization of the different coordinate systems and their relations.

One of the two transformations $\boldsymbol{Q}$ and $\boldsymbol{W}$ needs to be calibrated in an off-line procedure. We show below that the mathematical framework associated with this system is the same as that known as *hand–eye calibration* by the vision and robotics community.

4. Calibration procedure

The transformation from world coordinate system $\boldsymbol{O}_{\mathrm{W}}$ into the X-ray camera coordinate system $\boldsymbol{O}_{\mathrm{X}}$ for each image frame can be described by the external pose tracker,

$$\boldsymbol{T}_i = \boldsymbol{Q}\cdot\boldsymbol{S}_i\cdot\boldsymbol{W}^{-1}. \tag{5}$$

Determination of the two unknown homogeneous transformations,

$$\boldsymbol{Q}\in\mathbb{R}^{4\times4}:\boldsymbol{O}_{\mathrm{X}}\leftarrow\boldsymbol{O}_{\mathrm{T}},$$

$$\boldsymbol{W}\in\mathbb{R}^{4\times4}:\boldsymbol{O}_{\mathrm{W}}\leftarrow\boldsymbol{O}_{\mathrm{S}},$$

defines a mathematical problem, which turns out to be the same as a well-known calibration task in robotics called *hand–eye calibration*. A camera is mounted at the gripper of a robot whose pose can be controlled. In order to move the robot such that the camera adopts a certain position and orientation relative to the target, the relation between these two coordinate systems has to be determined. We describe the analogy between the two systems as follows. In our application, the 3D–3D transformation measured by the pose tracker is the equivalent of the robot's gripper pose, while the X-ray imaging system takes the place of the attached camera. This observation allows the use of several algorithms that have been proposed to solve the hand–eye calibration problem.

After having estimated one of the unknown transformations, we need to relate the sensor system measurements $\boldsymbol{S}_i$ to the projection geometry we want to determine. The X-ray projection geometry is defined in Eq. (2) as the product of the intrinsic and extrinsic parameters,

$$\boldsymbol{P}_i^{\mathrm{X}} = \boldsymbol{A}_i\cdot\boldsymbol{T}_i. \tag{6}$$

According to Eq. (5) the extrinsic parameters are expressed by the sensor measurement,

$$\boldsymbol{P}_i^{\mathrm{X}} = \boldsymbol{A}_i\cdot\boldsymbol{Q}\cdot\boldsymbol{S}_i\cdot\boldsymbol{W}^{-1}. \tag{7}$$

Assuming that we have determined the extrinsic parameters and sensor measurement for the reference frame, Eq. (5) can be used to replace one of the unknown transformations (i.e. $\boldsymbol{W}$),

$$\boldsymbol{P}_i^{\mathrm{X}} = \boldsymbol{A}_i\cdot\boldsymbol{Q}\cdot\boldsymbol{S}_i\cdot\boldsymbol{S}_{\mathrm{ref}}^{-1}\cdot\boldsymbol{Q}^{-1}\cdot\boldsymbol{T}_{\mathrm{ref}}. \tag{8}$$

Applying the virtual detector concept using the intrinsic parameters of the reference frame for the virtual detector plane leads to

$$\boldsymbol{P}_i^{\mathrm{X}} = \boldsymbol{H}_i\cdot\boldsymbol{A}_{\mathrm{ref}}\cdot\boldsymbol{Q}\cdot\boldsymbol{S}_i\cdot\boldsymbol{S}_{\mathrm{ref}}^{-1}\cdot\boldsymbol{Q}^{-1}\cdot\boldsymbol{T}_{\mathrm{ref}}. \tag{9}$$

Here, the motion described by the external sensor system is described in the camera coordinate system. In order to use the last equation for recovery of the X-ray projection geometry, we would have to decompose the reference projection matrix $\boldsymbol{P}_{\mathrm{ref}}$ (Ganapathy, 1984; Faugeras, 1993). This is an unstable procedure, as pointed out by Horaud and Dornaika (1995) and Navab et al. (1998). In order to achieve a robust solution this decomposition should be avoided.

In Eq. (7) we can alternatively substitute $\boldsymbol{Q}$ instead of $\boldsymbol{W}$. This leads to

$$\begin{aligned}\boldsymbol{P}_i^{\mathrm{X}} &= \boldsymbol{A}_i\cdot\boldsymbol{T}_{\mathrm{ref}}\cdot\boldsymbol{W}\cdot\boldsymbol{S}_{\mathrm{ref}}^{-1}\cdot\boldsymbol{S}_i\cdot\boldsymbol{W}^{-1}\\ &= \boldsymbol{H}_i\cdot\boldsymbol{A}_{\mathrm{ref}}\cdot\boldsymbol{T}_{\mathrm{ref}}\cdot\boldsymbol{W}\cdot\boldsymbol{S}_{\mathrm{ref}}^{-1}\cdot\boldsymbol{S}_i\cdot\boldsymbol{W}^{-1}\\ &= \boldsymbol{H}_i\cdot\boldsymbol{P}_{\mathrm{ref}}\cdot\boldsymbol{W}\cdot\boldsymbol{S}_{\mathrm{ref}}^{-1}\cdot\boldsymbol{S}_i\cdot\boldsymbol{W}^{-1}.\end{aligned} \tag{10}$$

The determined motion is now expressed in the patient

world coordinate system. Note that, although in Eq. (6) the projection matrix is presented as the product of intrinsic and extrinsic parameters, we do not have to compute any intrinsic or extrinsic parameters, but use a reference projection matrix $\boldsymbol{P}_{\text{ref}}$. The resulting equation (10) reflects the general framework developed in Section 3.3.

A practical problem still remains. The relative position and orientation of the sensor world and patient world coordinate systems—described by $\boldsymbol{W}$—is not a rigid constraint.

As both $\boldsymbol{Q}$ and $\boldsymbol{W}$ are not *suitable*, we need to find another transformation between the involved coordinate systems that actually stays constant between the calibration and patient run. According to Horaud and Dornaika (1995) this problem can be solved by introducing the new transformation

$$\boldsymbol{V} \in \mathbb{R}^{4\times4} : \boldsymbol{O}_{\text{W}} \leftarrow \boldsymbol{O}_{\text{T}},$$

such that

$$\boldsymbol{Q} = \boldsymbol{T}_{\text{ref}} \cdot \boldsymbol{V}. \tag{11}$$

It is assumed that the extrinsic parameters are known for a particular image frame. In our application we assume the image frame to be the reference frame. It will be demonstrated below that explicit knowledge of the extrinsic parameters—the result of a projection matrix decomposition—is not necessary. This new transformation describes the relation between the patient world coordinate system and the tool plate coordinate system for the C-arm in the reference position. The transformation is constant between calibration and patient run as long as the tool plate stays attached to the C-arm. Replacing $\boldsymbol{Q}$ in Eq. (9) leads to

$$\begin{aligned}\boldsymbol{P}_i^{\text{X}} &= \boldsymbol{H}_i \cdot \boldsymbol{A}_{\text{ref}} \cdot \boldsymbol{Q} \cdot \boldsymbol{S}_i \cdot \boldsymbol{S}_{\text{ref}}^{-1} \cdot \boldsymbol{Q}^{-1} \cdot \boldsymbol{T}_{\text{ref}} \\ &= \boldsymbol{H}_i \cdot \boldsymbol{A}_{\text{ref}} \cdot \boldsymbol{T}_{\text{ref}} \cdot \boldsymbol{V} \cdot \boldsymbol{S}_i \cdot \boldsymbol{S}_{\text{ref}}^{-1} \cdot \boldsymbol{V}^{-1} \cdot \boldsymbol{T}_{\text{ref}}^{-1} \cdot \boldsymbol{T}_{\text{ref}} \\ &= \boldsymbol{H}_i \cdot \boldsymbol{P}_{\text{ref}} \cdot \boldsymbol{V} \cdot \boldsymbol{S}_i \cdot \boldsymbol{S}_{\text{ref}}^{-1} \cdot \boldsymbol{V}^{-1}. \end{aligned} \tag{12}$$

This, as in Eq. (10), perfectly reflects the framework developed in Section 3.3 using a transformation that is constant for the calibration and patient run.

We will now show how to determine the unknown transformation $\boldsymbol{V}$ from a series of calibration measurements. Different authors have proposed solutions using linear and non-linear systems (Shiu and Ahmad, 1989; Tsai and Lenz, 1989; Chou and Kamel, 1991; Horaud and Dornaika, 1995; Daniilidis, 1999). These algorithms use motion equations between pairs of image frames to solve for the two unknown transformations.

The motion of *the* C-arm between two arbitrary image frames is described by

$$\begin{aligned}\boldsymbol{T}_{\text{ref}} \cdot \boldsymbol{T}_i^{-1} &= \boldsymbol{Q} \cdot \boldsymbol{S}_{\text{ref}} \cdot \boldsymbol{W}^{-1} \cdot \boldsymbol{W} \cdot \boldsymbol{S}_i^{-1} \cdot \boldsymbol{Q}^{-1} \\ &= \boldsymbol{Q} \cdot \boldsymbol{S}_{\text{ref}} \cdot \boldsymbol{S}_i^{-1} \cdot \boldsymbol{Q}^{-1}. \end{aligned} \tag{13}$$

Replacing $\boldsymbol{Q}$ by $\boldsymbol{V}$ leads to

$$\begin{aligned}\boldsymbol{T}_{\text{ref}} \cdot \boldsymbol{T}_i^{-1} &= \boldsymbol{T}_{\text{ref}} \cdot \boldsymbol{V} \cdot \boldsymbol{S}_{\text{ref}} \cdot \boldsymbol{S}_i^{-1} \cdot \boldsymbol{V}^{-1} \cdot \boldsymbol{T}_{\text{ref}}^{-1}, \\ \boldsymbol{T}_i^{-1} \cdot \boldsymbol{T}_{\text{ref}} &= \boldsymbol{V} \cdot \boldsymbol{S}_{\text{ref}} \cdot \boldsymbol{S}_i^{-1} \cdot \boldsymbol{V}^{-1}. \end{aligned} \tag{14}$$

The left-hand side of Eq. (14) describes the motion of the X-ray camera between two image frames in world coordinates. This motion can be computed from the projection matrices directly. Traditionally, this is done by decomposing the projection matrices (Ganapathy, 1984; Faugeras, 1993) into extrinsic and intrinsic parameters and then computing the motion from the extrinsic parameters. As pointed out before, different authors (Horaud and Dornaika, 1995; Navab et al., 1998) have emphasized that the decomposition of projection matrices is an unstable process, and an approach for computing the motion between two image frames from projection matrices without decomposing them has been proposed using the *direct motion estimation* algorithm (Navab et al., 1998) similar to the approach of Horn (1987) and Besl and McKay (1992).

With

$$\boldsymbol{T}_{(i)} := \boldsymbol{T}_i^{-1} \cdot \boldsymbol{T}_{\text{ref}},$$

$$\boldsymbol{S}_{(i)} := \boldsymbol{S}_i^{-1} \cdot \boldsymbol{S}_{\text{ref}},$$

and $\boldsymbol{T}_{(i)}$, $\boldsymbol{S}_{(i)}$ and $\boldsymbol{V}$ being of the form

$$\begin{bmatrix} \mathbf{R} & \mathbf{t} \\ 0^{\text{T}} & 1 \end{bmatrix},$$

Eq. (14) can be split into a matrix and a vector equation,

$$\mathbf{R}_{T_{(i)}} \cdot \mathbf{R}_V = \mathbf{R}_V \cdot \mathbf{R}_{S_{(i)}}, \tag{15}$$

$$(\mathbf{R}_{T_{(i)}} - \mathbf{Id}_3) \cdot \mathbf{t}_V = \mathbf{R}_V \cdot \mathbf{t}_{S_{(i)}} - \mathbf{t}_{T_{(i)}}. \tag{16}$$

Two different strategies exist in order to solve the above two-equation system. Most approaches (Shiu and Ahmad, 1989; Chou and Kamel, 1991; Mitschke et al., 2000) regard the two equations as decoupled. First, the rotation equation (15), and then the translation equation (16) is solved using the resulting rotation.

Using the special properties of rotation matrices, Eq. (15) can be transformed into

$$\mathbf{r}_{T_{(i)}} = \mathbf{R}_V \cdot \mathbf{r}_{S_{(i)}}, \tag{17}$$

with $\mathbf{r}_{T_{(i)}}$ and $\mathbf{r}_{S_{(i)}}$ representing the eigenvectors (rotation axes) of $\mathbf{R}_{T_{(i)}}$ and $\mathbf{R}_{S_{(i)}}$. This equation system can be solved from two or more equations, either directly (Shiu and Ahmad, 1989), or representing the unknown rotation matrix $\mathbf{R}_V$ as a quaternion (Horaud and Dornaika, 1995). Eq. (15) can be directly transformed into a quaternion equation which is then solved using the constraint of a resulting unit quaternion (Chou and Kamel, 1991).

The translation is then estimated using a linear least-squares method solving the equation system according to

Eq. (16). Note that the matrix $(\mathbf{R}_{T_{(i)}} - \mathbf{Id}_3)$ has rank 2 and therefore cannot be inverted.

A few methods attempt to solve both equations simultaneously. Both Eqs. (15) and (16) can be combined and solved by a non-linear minimization (Horaud and Dornaika, 1995). Daniilidis (1999) uses dual quaternions, an algebraic representation from screw theory, to describe the motions. This leads to a simultaneous linear minimization of rotation and translation.

5. Experiments

This section presents the experimental results. We first describe the special setup that was necessary for the hand–eye calibration. We then evaluate the two approaches for the on-line recovery of the X-ray projection geometry. As we tested several hand–eye calibration algorithms, we also compare their performance with the external tracking system approach. We evaluate these methods both numerically and based on the visual result of 3D tomographic reconstruction. Note that these results present one of the first three-dimensional tomographic reconstruction results using an inexpensive mobile X-ray C-arm.

5.1. Calibration setup

During the examination the C-arm rotates around an axis going through the center of the volume of interest which is to be reconstructed. However, in order to be able to compute the necessary transformation matrices, we need the C-arm to have at least two rotational motions around different rotation axes (Tsai and Lenz, 1989). This is not a natural motion for a C-arm used for 3D reconstruction. Fortunately, this must only be done during the off-line calibration process. This is visualized in Fig. 5.

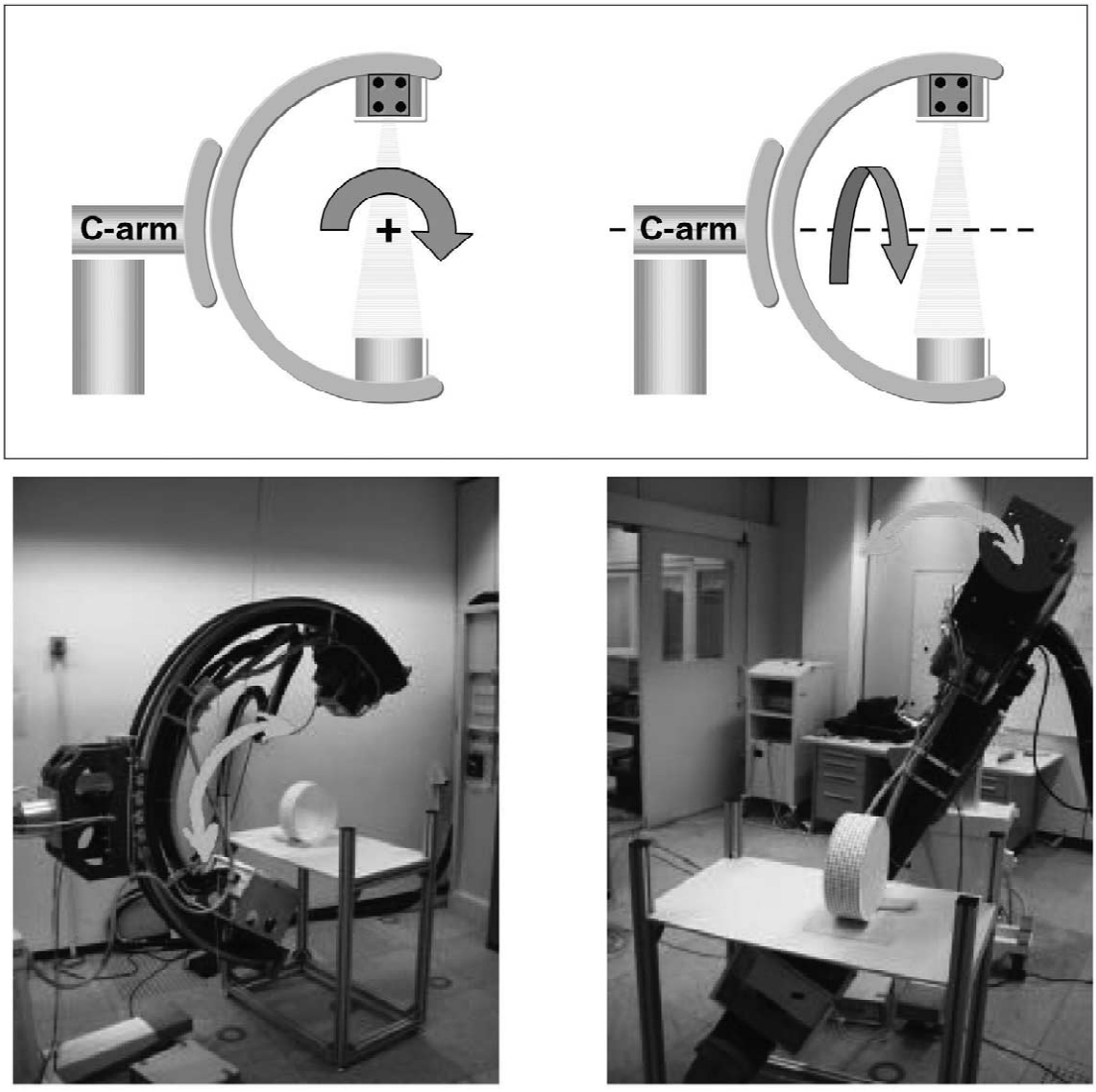

Fig. 5. Setup for calibration: C-arm in normal position during rotation (left) and in a special position (angulated) for the calibration procedure (right).

The image series used for calibration consists of 85 images of the normal patient run plus eight images where the C-arm is angulated. Direct recovery of the X-ray projection geometry—computing projection matrices $\boldsymbol{P}_i^{\mathrm{X}}$—is done using a cylindrical X-ray phantom as in (Navab et al., 1998). The calibration phantom is placed next to the object to be reconstructed such that the marker structure is visible in the X-ray images. The projection geometry is then recovered from these markers. In order to avoid reconstruction artefacts, the part of the image that is covered by the markers is removed before the reconstruction process. Note that this is not a practical scenario for use in the operating room. The so-determined set of projection matrices is used as *the gold standard* with which we will compare the other methods for both reconstruction results and numerical evaluation.

5.2. Reconstruction results

The set of projection matrices computed for each method is used to reconstruct a test phantom, visualized in Fig. 6. It consists of two cylindrical objects in an acrylic cover. Attached to it (not shown in Fig. 6) is a ring made from titanium alloy, also in an acrylic cover. We use a modified filtered backprojection reconstruction algorithm (Wiesent et al., 2000). The reconstruction results are shown in Figs. 7 and 8. Visualized are the three orthogonal Maximum Intensity Projections (MIP) of the reconstructed volume. The methods evaluated were:

- CAMC: camera-augmented C-arm, described in Section 3.4.
- CHOU: method of Chou and Kamel (1991), implementation courtesy of K. Daniilidis. (The rotation equation (15) is solved using a standard quaternion approach. With the resulting rotation matrix, the translation is determined from Eq. (16).)
- DANI: method of Daniilidis (1999), implementation courtesy of K. Daniilidis. (Both Eqs. (15) and (16) are solved simultaneously by describing the motion equations using dual quaternions.)
- HORlin: linear method proposed by Horaud and Dornaika (1995), based on (Shiu and Ahmad, 1989). (Eq. (17) is solved directly. With the resulting rotation matrix, the translation is determined from Eq. (16).)
- HORnlin: nonlinear method proposed by Horaud and Dornaika (1995), implementation courtesy of K. Daniilidis. (Eqs. (15) and (16) are combined and solved with a non-linear method.)
- TSAI: method of Tsai and Lenz (1989). (Rotation equation (17) is solved using an expression similar to the Rodrigues formula. With the resulting rotation matrix, the translation is determined from Eq. (16).)
- XRAY: *gold standard*, X-ray projection matrices obtained during patient run from calibration phantom.

All hand–eye calibration methods lead to *visually* satisfying results, and visually the differences in reconstruction quality are small. Nevertheless, both the gold standard of using the X-ray projection matrices and the CCD camera approach lead to better reconstruction quality than the external tracking system method.[1] Fig. 9 shows the reconstruction results of an anatomical object, a part of a pig's spine.

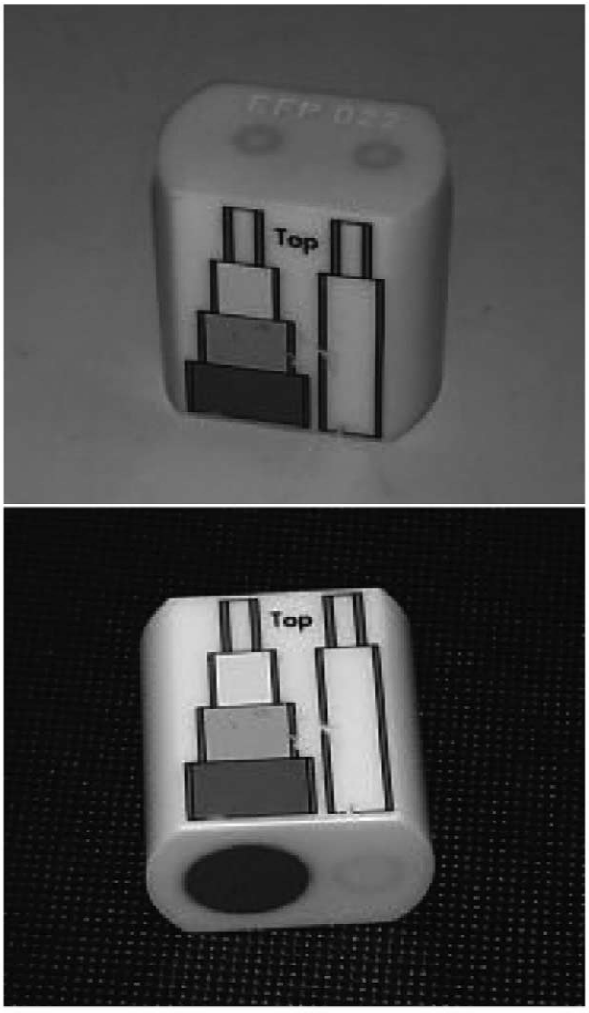

Fig. 6. The reconstruction phantom used in our evaluation: cylindrical objects in an acrylic cover. Attached to it is a ring made of titanium (not visible).

5.3. Numerical evaluation

Apart from the visual results we also want to compare the methods numerically. We compute the transformation (in the world coordinate system) between the projection matrices of each method and the corresponding gold standard X-ray projection matrix. The resulting errors for the absolute value of the angle of rotation and norm of translation are shown in Tables 1 and 2. At first glance the

[1] In order to draw this conclusion we asked 10 researchers, all experienced in 3D angiography, to independently visually assess the quality of the reconstructions.

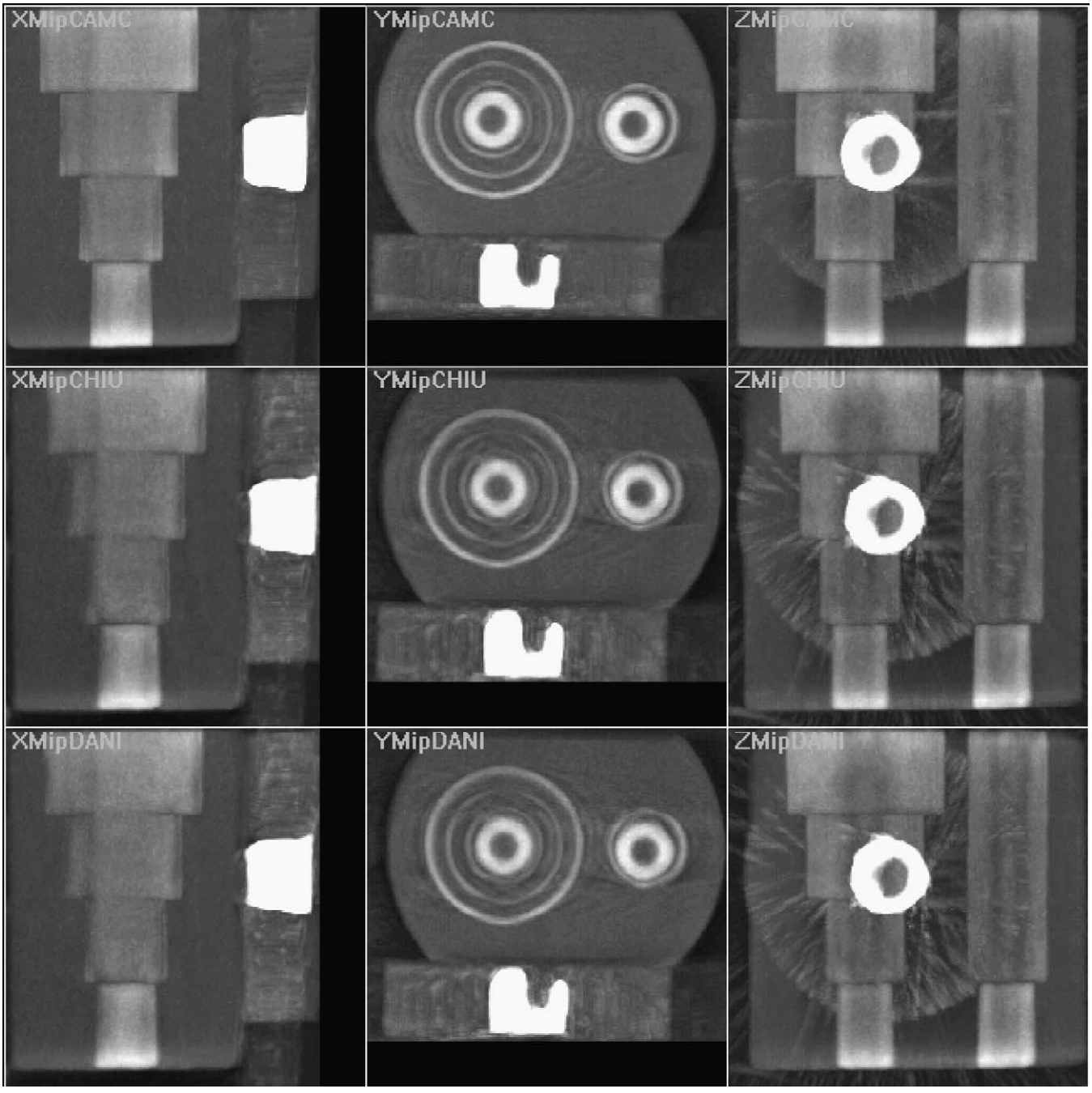

Fig. 7. Experimental results of 3D reconstruction using different calibration methods (from top to bottom): CAMC, CHOU, DANI.

errors for the sensor methods are smaller in both rotation and translation than for CAMC. This is surprising, because the quality of 3D reconstruction is better for CAMC than the external tracking system methods.

According to an experimental evaluation of the different optical tracking systems by Chassat and Lavallée (1998), we expect the mean error of the POLARIS system to be about $t_{\text{err}} \approx 0.6$ mm and $\theta_{\text{err}} \approx 0.25°$. This justifies the error in rotation, but only a part of the translation error.

The translation error can be decomposed into two components, translation in the direction of the optical axis of the X-ray system, and translation perpendicular to this axis. Translation along the optical axis has very little effect on the recovery of the projection geometry; this error parallel to the optical axis is of much less importance than the error perpendicular to the optical axis. If we compare the different methods based on the translation error perpendicular to the optical axis of the X-ray system (see Table 3), the CAMC method leads to better numerical results than the external sensor methods. This explains the better reconstruction quality. A large proportion of the error for CAMC is along the optical axis. This is not surprising, as

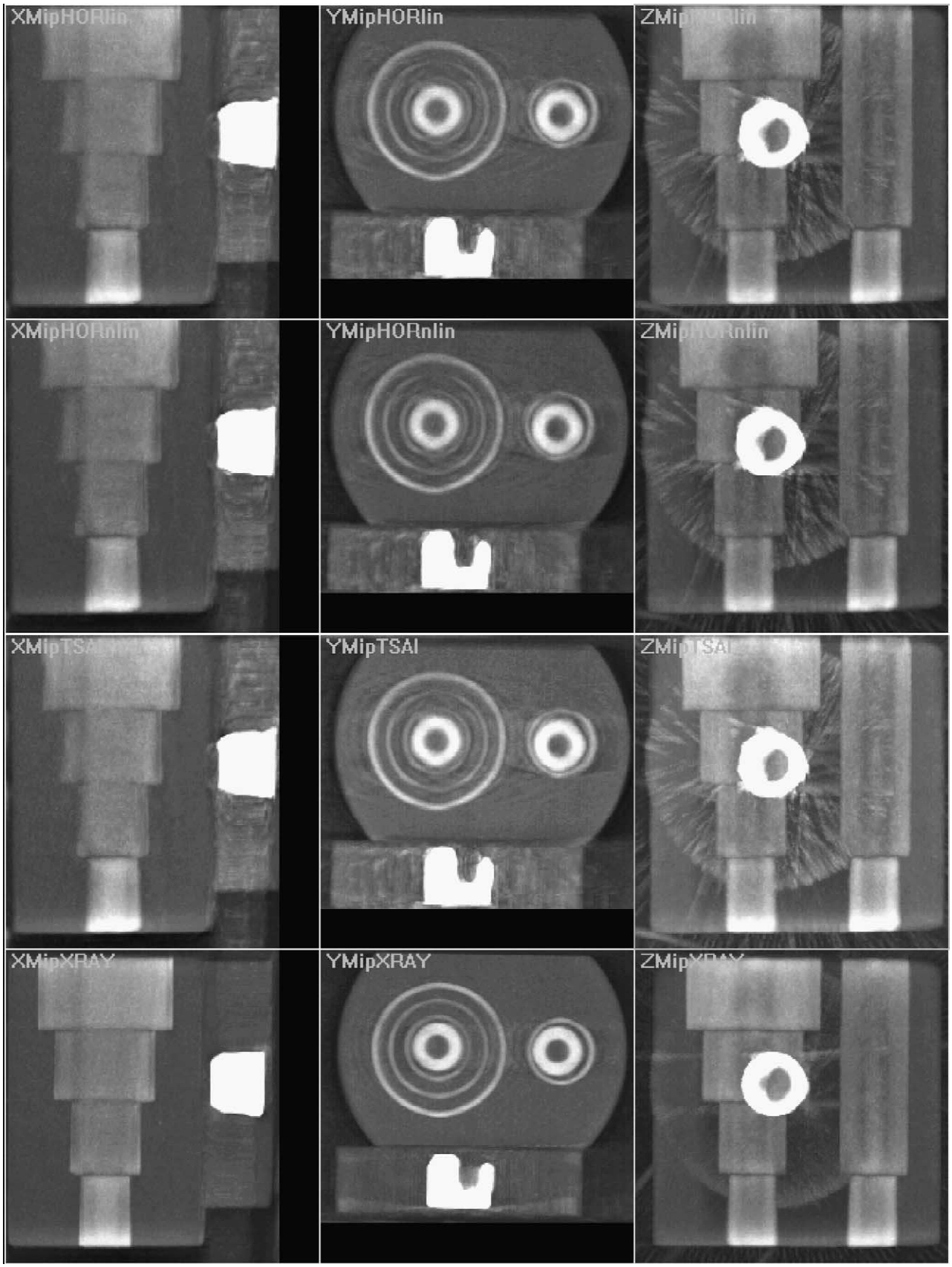

Fig. 8. Experimental results of 3D reconstruction using different calibration methods (from top to bottom): HORlin, HORnlin, TSAI, XRAY (gold standard).

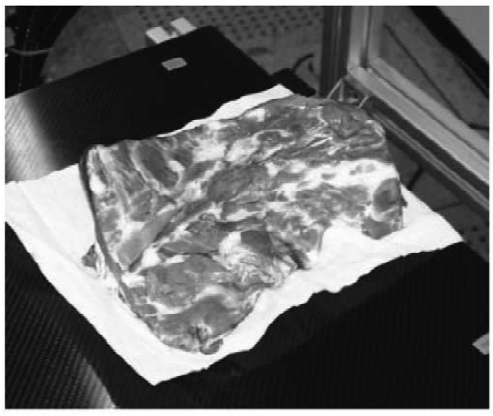

Experimental setup

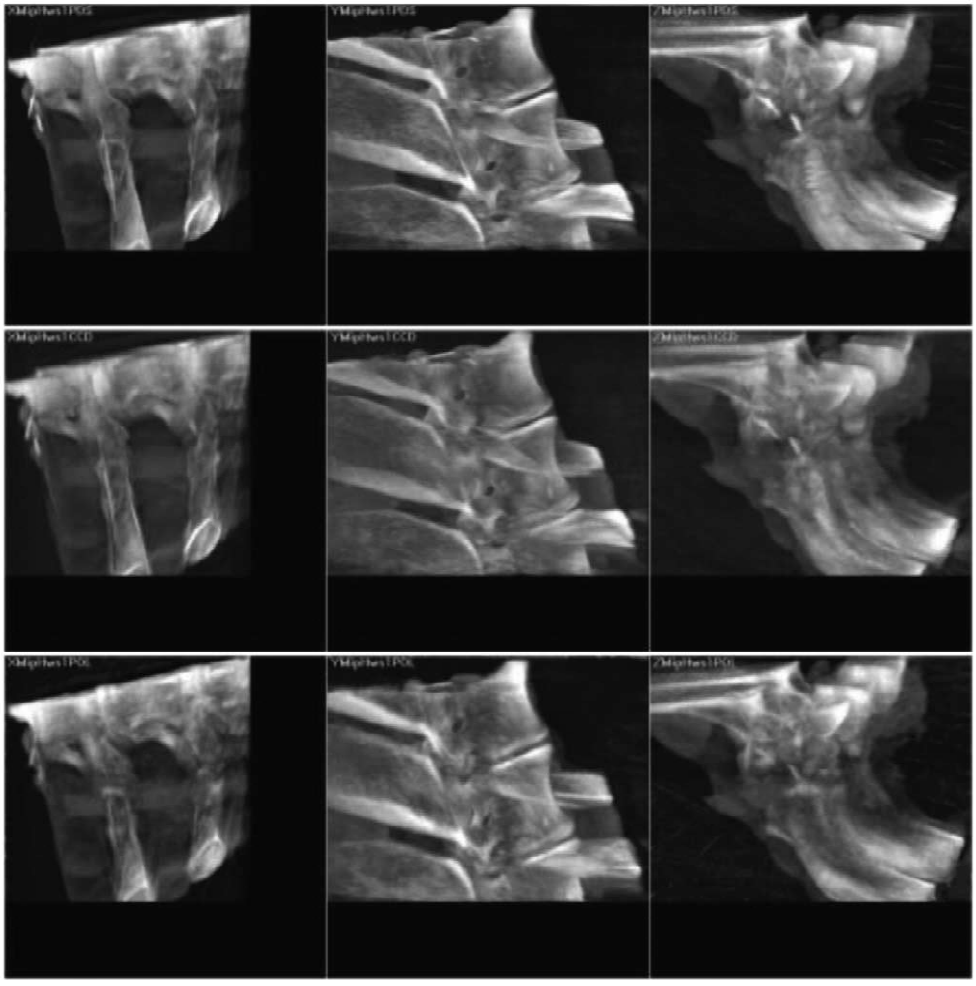

Fig. 9. Three-dimensional reconstruction of part of a pig's spine: three orthogonal Maximum Intensity Projections (MIP) of the reconstructed volume. Methods from top to bottom: gold standard, CAMC, and external tracking system.

Table 1
Comparison between external sensor and integrated camera method[a]

	CAMC	CHOU	DANI	HORlin	HORnlin	TSAI
μ	0.54	0.17	0.19	0.24	0.22	0.15
σ	0.20	0.07	0.06	0.11	0.09	0.07

[a] Rotation errors (in degrees).

Table 2
Comparison between external sensor and integrated camera method[a]

	CAMC	CHOU	DANI	HORlin	HORnlin	TSAI
μ	1.56	1.03	0.86	0.92	0.86	1.01
σ	0.20	0.65	0.53	0.60	0.57	0.55

[a] Translation errors (in mm).

Table 3
Comparison between external sensor and integrated camera method[a]

	CAMC	CHOU	DANI	HORlin	HORnlin	TSAI
t_{err}	1.56	1.03	0.86	0.92	0.86	1.01
$t_{\parallel\,opt}$	1.44	0.68	0.39	0.50	0.40	0.65
$t_{\perp\,opt}$	0.61	0.77	0.76	0.78	0.76	0.76

[a] Mean and standard deviation of translation error, t_{err}, error in the direction of the optical axis of the X-ray system, $t_{\parallel\,opt}$, and error perpendicular to the optical axis of the X-ray system, $t_{\perp\,opt}$ (in mm).

we expect most error to be along the optical axis of the attached CCD camera, which is almost parallel to the X-ray's optical axis. Although the stereo camera system of the pose tracker is much more precise in recovering the motion, its optical axis is always perpendicular to the optical axis of the X-ray system. So only a small fraction of the error is along the direction of the optical axis of the X-ray system, where it would have the least influence on the quality of the 3D reconstruction. There are only small differences between the different hand–eye calibration methods for the external tracking system approach.

6. Conclusion

In this paper we have presented a method for the use of external tracking or localization sensors for recovering the projection geometry of a moving X-ray system. This projection geometry is then used for 3D tomographic reconstruction. We first show that using external sensors for motion estimation is mathematically equivalent to the well-known hand–eye calibration problem. Then, we compare the results of X-ray geometrical calibration using external sensors with those obtained using a CCD camera attached to the X-ray source. These results are evaluated both in terms of the accuracy of motion estimation, and the quality of the final 3D reconstruction. Experimental results show that external sensors using hand–eye calibration methods provide a more accurate motion estimation. However, the quality of the 3D reconstruction is better when using the integrated CCD camera. This work clearly shows that the main part of the translation error for the integrated CCD camera is always towards the optical axis of both systems, and therefore has only a small influence on the quality of the 3D reconstruction. For the external sensor, the main part of the translation error is always perpendicular to the optical axis of the X-ray system, and therefore has a large influence on the quality of the 3D reconstruction. This conclusion is of major importance for both the medical imaging and augmented reality communities. The main message here is that the accuracy of calibration methods and apparatus should be defined only in terms of the goals of each particular application. In particular, for image back-projection for tomographic reconstruction, an integrated monocular imaging system performs the necessary geometrical calibration better than a professional and highly accurate (stereo-based) external sensor.

Mounting the CCD camera such that the optical axes of both the CCD camera and the X-ray imaging system are identical, leads to a minimal translational error perpendicular to the optical axis of the X-ray system. This setup is physically impossible, but can be accomplished by a double mirror system that bends the optical rays of the CCD camera such that both optical axes become identical (Mitschke and Navab, 2000b; Navab et al., 1999b; Mitschke et al., 2000). Our original setup is very similar to the proposed optimal setup, which is manifested in the very small differences between the numerical results for both setups.

For further reading, see (Lemke et al., 1995, 1997, 1999).

Acknowledgements

The authors would like to thank Kostas Daniilidis, Frank Sauer, Mariappan Nadar, Oliver Schütz, Rainer Graumann and Alok Gupta for active support and fruitful discussions. The authors would also like to thank Karl Wiesent and Wolfgang Seißler for providing the 3D reconstruction software.

Appendix A. Motion from projection matrices

This appendix explains how to estimate the motion between two image frames expressed by the two projection matrices describing the projection geometry. According to Eq. (2) the projection matrix $\boldsymbol{P}_i$ is composed of the matrix $\boldsymbol{A}_i$ containing the intrinsic parameters, and the matrix $\boldsymbol{E}_i$ containing the extrinsic parameters.

$$\boldsymbol{P}_i = \boldsymbol{A}_i \cdot \boldsymbol{T}_i. \tag{A.1}$$

The motion $\boldsymbol{T}_{ij}$ between two image frames i and j can be computed from the extrinsic parameters as follows:

$$\boldsymbol{T}_{ij} = \boldsymbol{T}_j^{-1} \cdot \boldsymbol{T}_i, \tag{A.2}$$

$$= \begin{pmatrix} \mathbf{R}_j^{\mathrm{T}} & -\mathbf{R}_j^{\mathrm{T}} \cdot \mathbf{t}_j \\ \mathbf{0}^{\mathrm{T}} & 1 \end{pmatrix} \cdot \begin{pmatrix} \mathbf{R}_i & \mathbf{t}_i \\ \mathbf{0}^{\mathrm{T}} & 1 \end{pmatrix}, \tag{A.3}$$

$$= \begin{pmatrix} \mathbf{R}_j^{\mathrm{T}} \cdot \mathbf{R}_i & \mathbf{R}_j^{\mathrm{T}}(\mathbf{t}_i - \mathbf{t}_j) \\ \mathbf{0}^{\mathrm{T}} & 1 \end{pmatrix}. \tag{A.4}$$

We first derive how to compute the rotation $\mathbf{R}_{ij} = \mathbf{R}_j^{\mathrm{T}} \cdot \mathbf{R}_i$ from the two matrices $\boldsymbol{M}_i$ and $\boldsymbol{M}_j$ composed of the first three column vectors of the projection matrices $\boldsymbol{P}_i$ and $\boldsymbol{P}_j$ such that

$$\boldsymbol{M}_i := \boldsymbol{A}_i \cdot \mathbf{R}_i, \tag{A.5}$$

where $\boldsymbol{A}_i$ is the 3×3 matrix of the intrinsic parameters.

The rotation $\mathbf{R}_{ij}$ can then be derived from the singular value decomposition of the matrix $\boldsymbol{M}_j^{\mathrm{T}} \cdot \boldsymbol{M}_i$ as follows:

$$\boldsymbol{M}_j^{\mathrm{T}} \cdot \boldsymbol{M}_i = \mathbf{U} \cdot \boldsymbol{\Sigma} \cdot \boldsymbol{V}^{\mathrm{T}}, \tag{A.6}$$

$$\mathbf{R}_{ij} = \mathbf{U} \cdot \boldsymbol{V}^{\mathrm{T}}. \tag{A.7}$$

Proof.

$$\boldsymbol{M}_j^{\mathrm{T}} \cdot \boldsymbol{M}_i = \mathbf{R}_j^{\mathrm{T}} \cdot \boldsymbol{A}_j^{\mathrm{T}} \cdot \boldsymbol{A}_i \cdot \mathbf{R}_i = \mathbf{U} \cdot \boldsymbol{\Sigma} \cdot \boldsymbol{V}^{\mathrm{T}}. \tag{A.8}$$

The intrinsic parameters of the two image frames can be assumed constant for CCD cameras or when using the virtual detector concept as described in Section 3.2 for X-ray images,

$$\boldsymbol{M}_j^{\mathrm{T}} \cdot \boldsymbol{M}_i = \mathbf{R}_j^{\mathrm{T}} \cdot \boldsymbol{A}^{\mathrm{T}} \cdot \boldsymbol{A} \cdot \mathbf{R}_i = \mathbf{U} \cdot \boldsymbol{\Sigma} \cdot \boldsymbol{V}^{\mathrm{T}}. \tag{A.9}$$

The singular value decomposition of the symmetric matrix $\boldsymbol{A}^{\mathrm{T}} \cdot \boldsymbol{A}$ is defined as

$$\boldsymbol{A}^{\mathrm{T}} \cdot \boldsymbol{A} = \mathbf{U}_A \cdot \boldsymbol{\Sigma}_A^2 \cdot \mathbf{U}_A^{\mathrm{T}}, \tag{A.10}$$

which, due to the uniqueness of the singular value decomposition, leads to

$$\mathbf{R}_j^{\mathrm{T}} \cdot \mathbf{U}_A \cdot \boldsymbol{\Sigma}_A^2 \cdot \mathbf{U}_A^{\mathrm{T}} \cdot \mathbf{R}_i = \mathbf{U} \cdot \boldsymbol{\Sigma} \cdot \boldsymbol{V}^{\mathrm{T}}, \tag{A.11}$$

$$(\mathbf{R}_j^{\mathrm{T}} \cdot \mathbf{U}_A) \cdot \boldsymbol{\Sigma}_A^2 \cdot (\mathbf{U}_A^{\mathrm{T}} \cdot \mathbf{R}_i) = \mathbf{U} \cdot \boldsymbol{\Sigma} \cdot \boldsymbol{V}^{\mathrm{T}}, \tag{A.12}$$

such that the product $\mathbf{U} \cdot \boldsymbol{V}^{\mathrm{T}}$ finally leads to

$$\mathbf{U} \cdot \boldsymbol{V} = \mathbf{R}_j^{\mathrm{T}} \cdot \mathbf{U}_A \cdot \mathbf{U}_A^{\mathrm{T}} \cdot \mathbf{R}_i = \mathbf{R}_j^{\mathrm{T}} \cdot \mathbf{R}_i. \quad \square \tag{A.13}$$

References

Azuma, R., 1997. A survey of augmented reality. Presence: Teleoperators and Virtual Environment 6 (4), 355–385.

Besl, P.J., McKay, N.D., 1992. A method for registration of 3-D shapes. IEEE Trans. Pattern Anal. Mach. Intell. 14 (2), 239–256.

Birkfellner, W., Watzinger, F., Wanschitz, F., Ewers, R., Bergmann, H., 1998. Calibration of tracking systems in a surgical environment. IEEE Trans. Med. Imaging 17 (5), 737–741.

Birkfellner, W., Huber, K., Watzinger, F., Figl, M., Wanschitz, F., Hanel, R., Rafolt, D., Ewers, R., Bergmann, H., 2000. Development of the varisocope-AR, a see-through HMD for computer-aided surgery. In: IEEE and ACM International Symposium on Augmented Reality, ISAR 2000, Munich, Germany.

Chassat, F., Lavallée, S., 1998. Experimental protocol of accuracy evaluation of 6-D localizers for computer-integrated surgery: Application to four optical localizers. In: Wells, W.W., Colchester, A., Delp, S.L. (Eds.), First International Conference on Medical Image Computing and Computer-Assisted Intervention (MICCAI), Cambridge, MA, pp. 277–284.

Chou, J., Kamel, M., 1991. Finding the position and orientation of a sensor on a robot manipulator using quaternions. Int. J. Robotics Res. 10 (3), 240–254.

Daniilidis, K., 1999. Hand–eye calibration using dual quaternions. Int. J. Robotics Res. 18 (3), 286–298.

Delp, S.L., Colchester, A. (Eds.), 1999. Medical Image Computing and Computer-Assisted Intervention – MICCAI. Lecture Notes in Computer Science, Vol. 1679. Springer, Berlin.

Delp, S.L., DiGioia, A.M., Jaramaz, B. (Eds.), 2000. Medical Image Computing and Computer-Assisted Intervention—MICCAI. Lecture Notes in Computer Science, Vol. 1935. Springer, Berlin.

Fahrig, R., Moreau, M., Holdsworth, D.W., 1997. Three-dimensional computer tomographic reconstruction using a C-arm mounted XRII: Correction of image intensifier distortion. Med. Phys. 24, 1097–1106.

Faugeras, O.D., 1993. Three-Dimensional Computer Vision: A Geometric Viewpoint. MIT Press, Cambridge, MA.

Feldkamp, L.A., Davies, L.C., Kress, J.W., 1984. Practical cone-beam algorithm. J. Opt. Soc. Am. A 6, 612–619.

Ganapathy, S., 1984. Decomposition of transformation matrices for robot vision. In: Proceedings of an IEEE International Conference on Robotics and Automation, pp. 130–139.

Groneschild, E., 1997. The accuracy and reproducibility of a global distortion in the X-ray imaging chain. Med. Phys. 24, 1875–1888.

Hoff, W.A., 1998. Fusion of data from head-mounted and fixed sensors. In: IEEE International Workshop on Augmented Reality, San Francisco, CA.

Horaud, R., Dornaika, F., 1995. Hand–eye calibration. Int. J. Robotics Res. 14 (3), 195–210.

Horn, B., 1987. Closed-form solution of absolute orientation using unit quaternions. J. Opt. Soc. Am. A 7, 629–642.

ImageOverlay, 1998 (http://www.mrcas.ri.cmu.edu/projects/overlay.html).

Kak, A.C., Jakowatz, C.V., Baily, N.A., Keller, R.A., 1977. Computerized tomography using video recorded fluoroscopy images. IEEE Trans. Biomed. Eng. 24, 157–169.

Koppe, P., Klotz, E., Op de Beek, J., Aerts, H., 1995. 3D vessel reconstruction based on rotational angiography. In: Lemke, H.U., Inamura, K., Jaffe, C.C., Vannier, M.W. (Eds.), Proceedings of Computer Assisted Radiology (CAR'95), pp. 101–107.

Koppe, P., Klotz, E., Aerts, H., Op de Beek, J., Kemkers, R., 1997. 3D reconstruction of cerebral vessel malformations based on rotational angiography (RA). In: Lemke, H.U., Vannier, M.W., Inamura, K. (Eds.), Proceedings of Computer Assisted Radiology and Surgery – CAR'97, pp. 145–151.

Kruger, R.A., Reineke, D.R., Smith, S.W., Ning, R., 1987. Reconstruction of blood vessels from X-ray subtraction images: limited angle tomography. Med. Phys. 14 (6), 940–949.

Lemke, H.U., Inamura, K., Jaffe, C.C., Vannier, M.W. (Eds.), 1995. Computer Assisted Radiology and Surgery – CAR'95. Elsevier, Amsterdam.

Lemke, H.U., Vannier, M.W., Inamura, K. (Eds.), 1997. Computer Assisted Radiology and Surgery – CAR'97. Excerpta Medica International Congress Series, Vol. 1134. Elsevier, Amsterdam.

Lemke, H.U., Vannier, M.W., Inamura, K., Farman, A.G. (Eds.), 1999. Computer Assisted Radiology and Surgery – CAR'99. Excerpta Medica International Congress Series, Vol. 1191. Elsevier, Amsterdam.

Mitschke, M., Navab, N., 2000a. Recovering projection geometry: how a cheap camera can outperform an expensive stereo system. In: Proceedings of the IEEE Conference on Computer Vision and Pattern Recognition, Hilton Head, SC, pp. 193–200, Vol. 1.

Mitschke, M., Navab, N., 2000b. Optimal configuration for dynamic calibration of projection geometry of X-ray C-arm systems. In: IEEE Workshop on Mathematical Methods in Biomedical Image Analysis, Hilton Head, SC, pp. 204–209.

Mitschke, M., Bani-Hashemi, A., Navab, N., 2000. Interventions under video-augmented X-ray guidance: application to needle placement. In: Delp, S.L., DiGioia, A.M., Jaramaz, B. (Eds.), Third International Conference on Medical Image Computing and Computer-Assisted Intervention (MICCAI), Pittsburgh, PA, pp. 858–868.

Navab, N., 2001. Method and apparatus using a virtual detector for three-dimensional reconstruction from X-ray images. United States Patent 6,236,704.

Navab, N., Bani-Hashemi, A., Mitschke, M., Holdsworth, D.W., Fahrig, R., Fox, A.J., Graumann, R., 1996. Dynamic geometrical calibration for 3D cerebral angiography. In: Proceedings of a SPIE Conference on Medical Imaging (2708), Newport Beach, CA, pp. 361–370.

Navab, N., Bani-Hashemi, A., Nadar, M., Wiesent, K., Durlak, P., Brunner, T., Barth, K., Graumann, R., 1998. 3D reconstruction from projection matrices in a C-arm based 3D-angiography system. In: Wells, W.W., Colchester, A., Delp, S.L. (Eds.), First International Conference on Medical Image Computing and Computer-Assisted Intervention (MICCAI), Cambridge, MA, pp. 119–129.

Navab, N., Mitschke, M., Schütz, O., 1999a. Camera augmented mobile C-arm (CAMC) application: 3D reconstruction using a low-cost mobile C-arm. In: Delp, S.L., Colchester, A. (Eds.), Second International Conference on Medical Image Computing and Computer-Assisted Intervention (MICCAI), Cambridge, UK, pp. 688–697.

Navab, N., Mitschke, M., Bani-Hashemi, A., 1999b. Merging visible and invisible: two camera-augmented mobile C-arm (CAMC) applications. In: IEEE International Workshop on Augmented Reality, San Francisco, CA, pp. 134–141.

Northern Digital, 2001. ON, Canada (http://www.ndi.ca).

Rougée, A., Picard, A.C., Ponchut, C., Trousset, Y., 1993. Geometrical calibration of X-ray imaging chains for three-dimensional reconstruction. Comput. Med. Imaging Graph. 17 (4/5), 295–300.

Shiu, Y.C., Ahmad, S., 1989. Calibration of wrist-mounted robotic sensors by solving homogeneous transform equations of the form AX = XB. IEEE Trans. Robotics Automation 5 (1), 16–29.

Tamamura, H., Yamamoto, H., Katayama, A., 1999. Steps towards seamless mixed reality. In: Proceedings of the First International Symposium on Mixed Reality.

Trousset, Y., Vaillant, R., Launay, L., Obadia, J.-M., Pivet, N., Anxionnat, R., Picard, C., 1999. A fully automated system for three-dimensional X-ray angiography. In: Lemke, H.U., Vannier, M.W., Inamura, K., Farman, A.G. (Eds.), Proceedings of Computer Assisted Radiology and Surgery (CAR'99), Paris, France, pp. 39–43.

Tsai, R.Y., Lenz, R.K., 1989. A new technique for fully autonomous and efficient 3D robotics hand/eye calibration. IEEE Trans. Robotics Automation 5 (3), 345–358.

Tuy, H., 1983. An inversion formula for cone-beam reconstruction. SIAM J. Appl. Math. 43, 546–552.

Wells, W.W., Colchester, A., Delp, S.L. (Eds.), 1998. Medical Image Computing and Computer-Assisted Intervention – MICCAI. Lecture Notes in Computer Science, Vol. 1496. Springer, Berlin.

Wiesent, K., Barth, K., Navab, N., Durlak, P., Brunner, T., Schütz, O., Seissler, W., 2000. Enhanced 3-D-reconstruction algorithm for C-arm systems suitable for interventional procedures. IEEE Trans. Med. Imaging 19 (5), 391–403.